JACS
JOURNAL OF THE AMERICAN CHEMICAL SOCIETY
Article
Cite This: J. Am. Chem. Soc. 2019, 141, 15710−15716
pubs.acs.org/JACS

Tuning the Structure and Chiroptical Properties of Gold Nanoparticle Single Helices via Peptide Sequence Variation

Soumitra Mokashi-Punekar,[†] Tiffany R. Walsh,*[,§] and Nathaniel L. Rosi*[,†,‡]

[†]Department of Chemistry, and [‡]Department of Chemical and Petroleum Engineering, University of Pittsburgh, Pittsburgh, Pennsylvania 15260, United States

[§]Institute for Frontier Materials, Deakin University, Geelong, Victoria 3216, Australia

Supporting Information

ABSTRACT: Just as peptide function is determined by the position, sequence, and overall arrangement of constituent amino acids, the optical properties of nanoparticle (NP) assemblies are influenced by the size, dimensions, and arrangement of constituent NPs. In this work, we demonstrate that peptide sequence can be programmed to direct the structure and chiroptical activity of chiral helical gold NP (AuNP)superstructures, a growing class of chiral nanomaterials with potential in sensing, detection, and optics-based applications. Gold-binding peptide conjugate families, C_{18}-$(PEP_{Au}{}^{M,x})_2$ and C_{18}-$(PEP_{Au}{}^{M\text{-}ox,x})_2$, that differ in the position (x = 7, 9, and 11) of methionine (M)/methionine sulfoxide (M-ox) within the peptide sequences (PEP_{Au} = AYSSGAPPMPPF/$PEP_{Au}{}^{M\text{-}ox}$ = AYSSGAPPM^{ox}PPF) are employed to control the aspect ratio and size of AuNPs within helical NP assemblies. Computational modeling reveals that the amino acid variations have a profound effect on peptide−AuNP interactions that ultimately lead to control over NP size. C_{18}-$(PEP_{Au}{}^{M,x})_2$ (x = 7, 9, and 11) yield irregular double-helical superstructures comprising spherical AuNPs, while C_{18}-$(PEP_{Au}{}^{M\text{-}ox,x})_2$ (x = 9, 11) yield single-helical assemblies comprising oblong or rod-shaped AuNPs. Further, component AuNPs are larger when M/M-ox is placed at x = 11, while smaller component AuNPs are observed when M/M-ox is placed at x = 7. Changes in nanoscale structures manifest themselves in observable differences in chiroptical signal intensity. Ultimately, we achieve dramatic variance in the structure and properties of chiral AuNP superstructures via simple molecular-level tuning of peptide primary sequence.

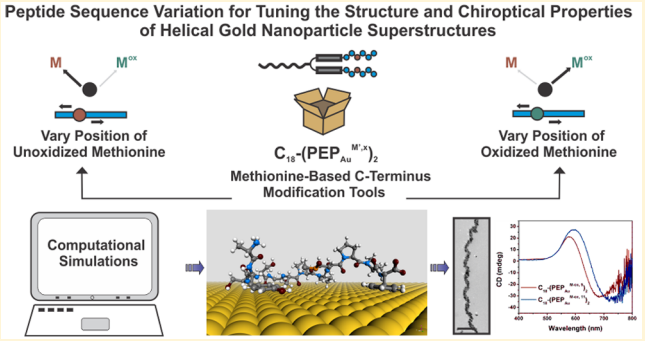

INTRODUCTION

The placement and positioning of chemical building blocks, whether they be atoms within molecules or molecules within molecular assemblies, define the properties and functions of the chemical or material entity. Chemists, as architects of the molecular landscape, can finely control molecular composition and structure and, in many cases, "dial in" properties with great accuracy and deliberate intent. Like molecules and molecular architectures, the placement and organization of nanoparticles within larger-scale nanoparticle superstructures also dramatically affects superstructure properties and function.[1]

Chiral helical gold nanoparticle (AuNP) superstructures are an exciting class of materials[2] that have potential for wide-ranging applications in chemical sensing,[3] catalysis,[4] and optics.[5] Strong plasmonic chiroptical activity is required to realize many of these proposed applications. Theoretical studies indicate that the chiroptical signal intensity for such structures depends on many factors, including the helical pitch and the size of the component nanoparticles.[6]

We have developed highly modular molecular methods for synthesizing and assembling nanoparticles.[2a,e,7,8] Here, precursor peptide constructs direct nanoparticle synthesis and assembly. The peptide constructs constitute tunable molecular species that can be carefully designed to finely control superstructure morphology, metrics, and, ultimately, properties. Our construct designs are largely based on the "A3" gold-binding peptide (AYSSGAPPMPPF),[9] which we refer to in our studies as "PEP_{Au}". We have designed a broad spectrum of R−PEP_{Au} conjugates for preparing a diverse collection of nanoparticle assemblies, in particular chiral helical gold nanoparticle superstructures.[2a,e,g,7a,d,10] Our prior studies have largely focused on variation of the "R" group. The peptide sequence represents a more complex molecular handle whose influence on nanoparticle superstructure architecture is largely unexplored. Through a combination of theory and experiment, we present herein the first steps toward realizing the design of programmable peptide units whose sequences encode and define the phenotype (e.g., structure, metrics, and properties) of a product nanoparticle superstructure.

We have previously prepared AuNP double helices[10b] and single helices[2g] using C_{18}-$(PEP_{Au})_2$ and C_{18}-$(PEP_{Au}{}^{M\text{-}ox})_2$,

Received: August 14, 2019
Published: September 5, 2019

DOI: 10.1021/jacs.9b08798
J. Am. Chem. Soc. 2019, 141, 15710−15716

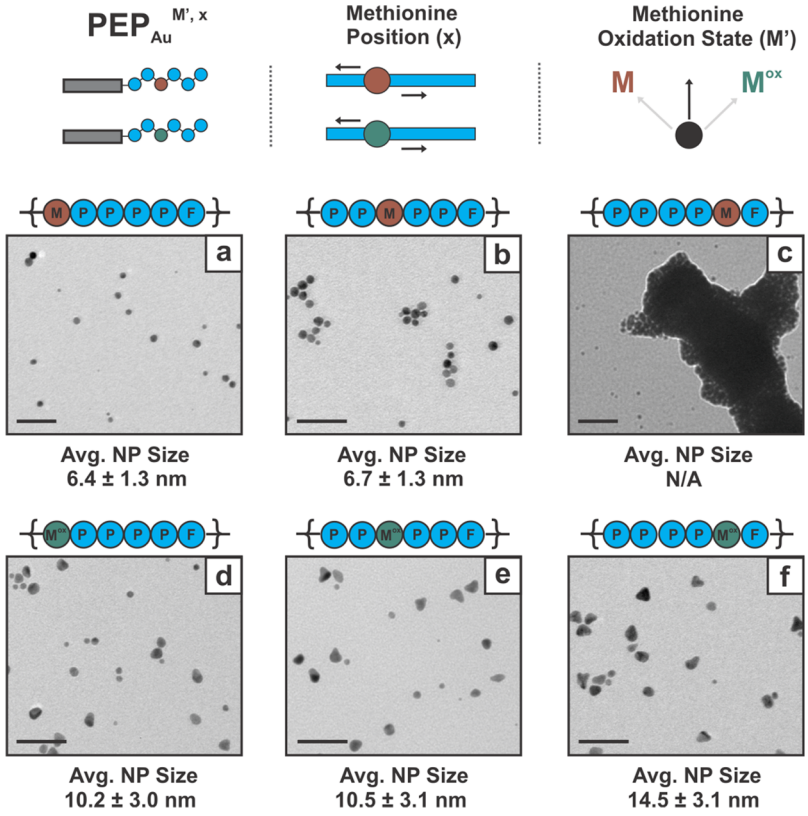

Figure 1. Effect of methionine oxidation and position on the size and shape of AuNPs. TEM images of AuNPs synthesized in the presence of (a) $PEP_{Au}^{M,7}$, (b) $PEP_{Au}^{M,9}$, (c) $PEP_{Au}^{M,11}$, (d) $PEP_{Au}^{M\text{-}ox,7}$, (e) $PEP_{Au}^{M\text{-}ox,9}$, and (f) $PEP_{Au}^{M\text{-}ox,11}$. Average AuNP size values are included below each TEM image. Scale bar: 100 nm.

respectively, divalent peptide conjugate molecules that consist of two PEP_{Au}/$PEP_{Au}^{M\text{-}ox}$ (AYSSGAPPM^{ox}PPF) sequences attached to a C_{18} aliphatic tail, where M-ox represents methionine sulfoxide. In aqueous media, both conjugates assemble into helical fibers. In the presence of Au salt and reducing agent, these molecules associate with in situ formed AuNPs and incorporate them into their assembled structure. Interestingly, C_{18}-$(PEP_{Au})_2$ directs the assembly of AuNPs into irregular double helices comprising spherical particles, while C_{18}-$(PEP_{Au}^{M\text{-}ox})_2$ directs the assembly of AuNPs into chiral well-defined single-helical superstructures composed primarily of rod-like particles. The methionine residue clearly plays an important role in both defining superstructure morphology and controlling particle size and dimensions. On the basis of our established assembly model,[2g] C_{18}-$(PEP_{Au}^{M\text{-}ox})_2$ assembles into helical ribbons such that the C-terminus (−PPM^{ox}PPF) interacts with the AuNPs anchored to the ribbon surface. Further, molecular dynamics simulations on PEP_{Au} identify methionine as a key amino acid that interacts strongly with AuNP surfaces.[11]

Taken together, these observations necessitate a comprehensive comparison of the Au-binding interactions of both oxidized and unoxidized peptides. The strong gold-binding affinity of methionine prompts us to question whether the position of the methionine/methionine sulfoxide within the C-terminus affects the peptide−Au interaction. We hypothesize that the position of both M and M-ox within the C-terminus will dictate the extent of gold binding, which in turn will affect the size and dimensions of both discrete and assembled AuNPs. We therefore predict that encoding chemical information via small methionine-based C-terminus modifications might allow us to tune the structural metrics of helical AuNP superstructures and reliably tailor their chiroptical properties.

RESULTS AND DISCUSSION

We designed and synthesized a series of variant peptide sequences, which vary in both the oxidation state and the position of the methionine residue (Figure S1). The unoxidized peptides are (i) NH_2-AYSSGAMPPPPF, (ii) NH_2-AYSSGAPPMPPF, and (iii) NH_2-AYSSGAPPPPMF, and the oxidized peptides are (iv) NH_2-AYSSGAM^{ox}PPPPF, (v) NH_2-AYSSGAPPM^{ox}PPF, and (vi) NH_2-AYSSGAPPPP-M^{ox}F. Hereafter, each variant peptide sequence is referred to by the methionine position and oxidation state (e.g., $PEP_{Au}^{M\text{-}ox,7}$ = NH_2-AYSSGAM^{ox}PPPPF and $PEP_{Au}^{M,9}$ = NH_2-AYSSGAPPMPPF). To determine how sequence and oxidation state affect particle size and dimensions, this collection of peptides was first used to prepare discrete peptide-capped NPs. Briefly, peptides were dissolved in HEPES buffer (4-(2-hydroxyethyl)-1-piperazinethanesulfonic acid) (pH = 7), which acts a reducing agent for gold ions.[12] Next, an aliquot of $HAuCl_4$/TEAA, the gold ion precursor solution, was added to the peptide solution. We determined using transmission electron microscopy (TEM) imaging that particles prepared with the unoxidized peptide sequences are predominantly spherical in nature. $PEP_{Au}^{M,7}$ and $PEP_{Au}^{M,9}$ both yield spherical NPs with average particle sizes of 6.4 ± 1.3 and 6.7 ± 1.3 nm, respectively. However, $PEP_{Au}^{M,11}$ yields large NP aggregates (Figure 1). Interestingly, the oxidized peptides do not follow these trends in NP size. $PEP_{Au}^{M\text{-}ox,7}$, $PEP_{Au}^{M\text{-}ox,9}$, and $PEP_{Au}^{M\text{-}ox,11}$ all yield larger nonspherical AuNPs (Figure 1).

DOI: 10.1021/jacs.9b08798
J. Am. Chem. Soc. 2019, 141, 15710−15716

The average particle size (longest dimension measured) for particles prepared in the presence of $PEP_{Au}^{M\text{-}ox,7}$ and $PEP_{Au}^{M\text{-}ox,9}$ is 10.2 ± 3.0 and 10.5 ± 3.1 nm, respectively. However, $PEP_{Au}^{M\text{-}ox,11}$ yields AuNPs with a larger average diameter of 14.5 ± 3.0 nm. These trends in average NP diameter were further confirmed via UV−vis spectroscopy. The localized surface plasmon resonance (LSPR) peak for particles prepared in the presence of $PEP_{Au}^{M,7}$ and $PEP_{Au}^{M,9}$ is located at 519 and 525 nm. However, LSPR peaks for AuNPs synthesized in the presence of $PEP_{Au}^{M\text{-}ox,7}$, $PEP_{Au}^{M\text{-}ox,9}$, and $PEP_{Au}^{M\text{-}ox,11}$ are much broader and red-shifted (Figure S3).

We used theoretical modeling to assist in understanding these results. We started by first comparing the binding energy of small molecules on the surface of Au(111). van der Waals density functional theory (vdW-DF)[13] calculations of dimethyl sulfoxide (DMSO) adsorbed on the Au(111) surface in vacuo predict the binding energy to be −55 kJ/mol as compared to −77 kJ/mol for dimethyl sulfide. Using the unmodified parameters of the polarizable GolP-CHARMM force-field, we found a consistent trend, with a calculated in vacuo binding energy of −42 ± 10 kJ/mol for DMSO, as compared to our previously reported value of −70 kJ/mol for dimethyl sulfide.[14] These preliminary data on small molecule counterparts suggest that the oxidized methionine has a weaker interaction with Au(111).

We proceeded to predict the degree of residue−surface contact for each residue within the modified and unmodified PEP_{Au} sequence adsorbed at the aqueous Au(111) interface. This characterization of peptide-surface adsorption is typically not an additive function of the peptide's constituent residues, due in part to the inherent intrinsic disorder of biocombinatorially selected materials-binding peptides in general. The adsorbed state of such peptides cannot be adequately captured by a single conformation, but instead is more appropriately represented by a conformational ensemble. To this end, we used replica-exchange with solute tempering molecular dynamics (REST-MD) simulations[15] in partnership with the GolP-CHARMM force-field[16] to predict the Boltzmann-weighted ensemble of conformations for each of the six surface adsorbed peptides in the presence of liquid water. REST-MD simulations of peptide-surface adsorption have been previously demonstrated to be highly effective, yielding binding results that are consistent with experimental data.[11a,17] We began by comparing the binding interactions of the unoxidized PEP_{Au} variant sequences, and we note that our predictions for $PEP_{Au}^{M,9}$ binding are consistent with previously reported modeling studies (comparison provided in the Supporting Information).

As compared to $PEP_{Au}^{M,9}$, both $PEP_{Au}^{M,7}$ and $PEP_{Au}^{M,11}$ exhibit a decrease in binding interaction of the methionine residue (Figure 2a−c). We relate this observation to the presence of 4 adjacent prolines (P), which result in a "mesogenic" rigid segment and therefore reduce the binding interaction of other residues. In the case of $PEP_{Au}^{M,7}$, the change in methionine position does not significantly affect the binding interactions of other amino acids. Therefore, the overall binding interactions of $PEP_{Au}^{M,9}$ and $PEP_{Au}^{M,7}$ are comparable. However, in the case of $PEP_{Au}^{M,11}$, the change in methionine position results in a global reduction of other neighboring amino acids. $PEP_{Au}^{M,11}$ displays the least binding interaction with Au(111) surface. We speculate that this observation could be due to the competing effects of adjacent M and F residues, which are both strong binders. Overall, the

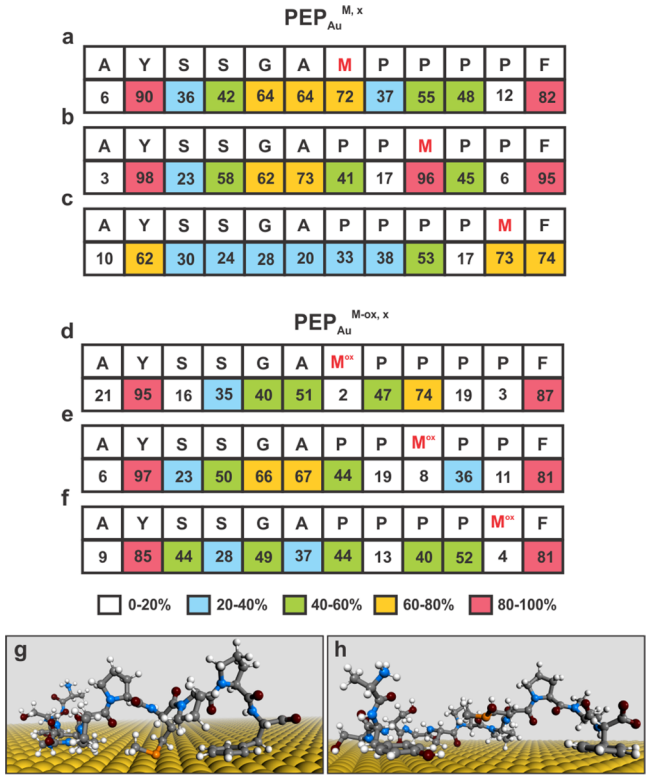

Figure 2. REST-MD simulations performed on oxidized and unoxidized peptide sequences. Average degree of residue−Au contact (given as a percentage of the REST-MD trajectory) is listed for each residue in all sequences. (a) $PEP_{Au}^{M,7}$, (b) $PEP_{Au}^{M,9}$ (data taken from ref 11b), (c) $PEP_{Au}^{M,11}$, (d) $PEP_{Au}^{M\text{-}ox,7}$, (e) $PEP_{Au}^{M\text{-}ox,9}$, and (f) $PEP_{Au}^{M\text{-}ox,11}$. Representative structures of (g) $PEP_{Au}^{M,9}$ and (h) $PEP_{Au}^{M\text{-}ox,9}$ adsorbed at the Au(111) interface as predicted from REST-MD simulations. The degree of contact between the Au(111) surface and the methionine sulfoxide (h) is drastically reduced as compared to the Au(111)−methionine interaction (g) (color code: C, gray; N, blue; O, dark red; H, white; S, orange).

theoretical binding interaction is in good agreement with the experimentally observed trends in AuNP sizes. Both $PEP_{Au}^{M,7}$ and $PEP_{Au}^{M,9}$ yield small spherical AuNPs. However, large AuNP aggregates are synthesized in the presence of $PEP_{Au}^{M,11}$.

Next, we compared the binding interactions of the oxidized PEP_{Au} variants. A common theme in all oxidized peptides regardless of methionine sulfoxide position is that the binding interaction of the methionine sulfoxide is dramatically low as compared to unoxidized methionine (Figure 2). For example, Figure 2g and h illustrates the comparative decrease in Au(111) surface contact between $PEP_{Au}^{M,9}$ and $PEP_{Au}^{M\text{-}ox,9}$, respectively. This observation is also consistent with the size discrepancy in discrete AuNPs synthesized using the oxidized and unoxidized PEP_{Au} sequences. Because AuNPs are formed by the in situ growth of smaller particles, peptide sequences having low Au binding interaction (i.e., oxidized sequences) would serve as weak surface capping agents and therefore facilitate the formation of larger AuNPs. As compared to $PEP_{Au}^{M\text{-}ox,9}$, both $PEP_{Au}^{M\text{-}ox,7}$ (Figure 2d) and $PEP_{Au}^{M\text{-}ox,11}$ (Figure 2f) exhibit a slight reduction in binding interaction. Similar to the unoxidized peptides, this can be attributed to the presence of four adjacent proline residues causing rigidity in the sequence. Although one might expect both $PEP_{Au}^{M\text{-}ox,7}$ and $PEP_{Au}^{M\text{-}ox,11}$ to yield larger AuNPs as compared to $PEP_{Au}^{M\text{-}ox,9}$, experimentally large particles are observed only in the case of

DOI: 10.1021/jacs.9b08798
J. Am. Chem. Soc. 2019, 141, 15710−15716

$PEP_{Au}^{M\text{-}ox,11}$. From both theory and experimental data, we conclude that (i) the oxidation of methionine dramatically decreases the peptide−AuNP binding interaction, and (ii) the proximity of M/M-ox to the C-terminus of the peptide sequence results causes either an increase in NP size or particle aggregation.

To confirm that the variations observed in the surface adsorption characteristics arise primarily due to the difference in the M-ox/M surface binding strength and not due to any differences inherent to the peptide conformational ensemble, we ran REST-MD simulations for each of the six sequences in the unadsorbed state. We characterized the resulting Boltzmann-weighted conformational ensemble of each of the six MD trajectories by using a clustering analysis. In general, this analysis identifies a set of like structures (referred to as clusters) and their fractional population in the ensemble. In this instance, our comparison was based on the structural similarity of the peptide backbone. We then used a cross-peptide analysis to compare the structural similarity of, for example, each cluster in the $PEP_{Au}^{M,7}$ ensemble to the set of clusters generated for $PEP_{Au}^{M\text{-}ox,7}$. The clusters for the $PEP_{Au}^{M,9}$/$PEP_{Au}^{M\text{-}ox,9}$ and $PEP_{Au}^{M,11}$/$PEP_{Au}^{M\text{-}ox,11}$ were similarly compared. Although the fractional populations of the clusters in each ensemble differ, we note a substantial degree of similarity between the backbone conformations for all three cases: $PEP_{Au}^{M,7}$/$PEP_{Au}^{M\text{-}ox,7}$, $PEP_{Au}^{M,9}$/$PEP_{Au}^{M\text{-}ox,9}$, and $PEP_{Au}^{M,11}$/$PEP_{Au}^{M\text{-}ox,11}$ (Tables S1−S9 and Figure 3). To

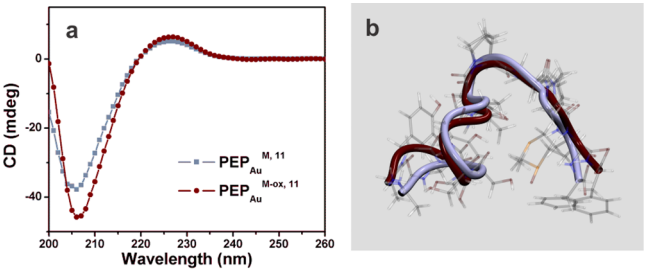

Figure 3. Secondary structure analysis of $PEP_{Au}^{M,11}$ and $PEP_{Au}^{M\text{-}ox,11}$. (a) CD measurements indicate that both $PEP_{Au}^{M,11}$ and $PEP_{Au}^{M\text{-}ox,11}$ exhibit predominantly PPII secondary conformations in solution. (b) Structural similarity between $PEP_{Au}^{M,11}$ (blue) and $PEP_{Au}^{M\text{-}ox,11}$ (red) sequences gathered via theoretical cross-peptide analysis.

further validate these theoretical findings with experimental data, we studied the secondary structure of all peptides in HEPES buffer in the absence of gold (unadsorbed state). Circular dichroism (CD) spectra indicate that all peptides exhibit polyproline II secondary structure (Figures 3 and S4). We calculated the Ramachandran plot for each peptide in the unadsorbed state, based on the entire REST-MD trajectory in each case. Consistent with the CD spectra, every peptide was predicted to feature a substantial contribution from the polyproline II secondary structure (Table S10).

Encouraged by the effects of peptide C-terminus modification on the size of discrete AuNPs, we next investigated the effects of the methionine-based modifications on the size of component AuNPs within the helical superstructures. Azido-modified variant divalent peptide conjugates were synthesized (e.g., N_3-AYSSGAPPM^{ox}PPF) and coupled to a dialkyne modified C_{18} aliphatic tail via copper-catalyzed click chemistry (see Experimental Methods and Figure S2). Unoxidized peptide conjugates [C_{18}-$(PEP_{Au}^{M,7})_2$, C_{18}-$(PEP_{Au}^{M,9})_2$, and C_{18}-$(PEP_{Au}^{M,11})_2$] and oxidized peptide conjugates [C_{18}-$(PEP_{Au}^{M\text{-}ox,7})_2$, C_{18}-$(PEP_{Au}^{M\text{-}ox,9})_2$, and C_{18}-$(PEP_{Au}^{M\text{-}ox,11})_2$] were subjected to our established AuNP assembly conditions.[2g] C_{18}-$(PEP_{Au}^{M,7})_2$, C_{18}-$(PEP_{Au}^{M,9})_2$, and C_{18}-$(PEP_{Au}^{M,11})_2$ all form one-dimensional AuNP assemblies with irregular helicity (Figures 4 and S5). The overall superstructure morphology observed in these cases is consistent with our previous studies.[10b] In all three cases, the assemblies are composed primarily of spherical particles. The average diameter of component AuNPs in C_{18}-$(PEP_{Au}^{M,7})_2$- and C_{18}-$(PEP_{Au}^{M,9})_2$-based superstructures is 8.1 ± 1.9 and 9.0 ± 1.8 nm, respectively. The large majority of helical superstructures derived from C_{18}-$(PEP_{Au}^{M,11})_2$ consist of larger spherical particles that have average diameters equal to 12.3 ± 1.7 nm.

Before studying the assembly of AuNPs using the oxidized peptide conjugates, we determined the morphology of the C_{18}-$(PEP_{Au}^{M\text{-}ox,7})_2$ and C_{18}-$(PEP_{Au}^{M\text{-}ox,11})_2$ fibers. Atomic force microscopy (AFM) revealed that C_{18}-$(PEP_{Au}^{M\text{-}ox,7})_2$ and C_{18}-$(PEP_{Au}^{M\text{-}ox,11})_2$ assemble into helical ribbons with average helical pitch values of 91 ± 6 and 93 ± 7 nm (Figure S6), which is consistent with fibers formed using C_{18}-$(PEP_{Au}^{M\text{-}ox,9})_2$.[2g] These data confirm that the position of M-ox within the peptide C-terminus does not affect the morphology of the helical ribbons. C_{18}-$(PEP_{Au}^{M\text{-}ox,9})_2$ and C_{18}-$(PEP_{Au}^{M\text{-}ox,11})_2$-based syntheses yield well-defined single-helical superstructures (Figures 4 and S8), while C_{18}-$(PEP_{Au}^{M\text{-}ox,7})_2$ yields only unassembled, discrete AuNPs (Figure S7). The component AuNPs in the single-helical superstructures are oblong in shape. The average length and width of AuNPs in helices constructed using C_{18}-$(PEP_{Au}^{M\text{-}ox,9})_2$ are 15.5 ± 3.5 and 8.8 ± 2.5 nm, respectively. Interestingly, C_{18}-$(PEP_{Au}^{M\text{-}ox,11})_2$ yields single helices with larger component AuNPs. The average AuNP length and width measured in this case are 20.5 ± 3.1 and 8.3 ± 1.8 nm, respectively. Although the inability of C_{18}-$(PEP_{Au}^{M\text{-}ox,7})_2$ to direct the assembly single-helical superstructures warrants further investigation, the observed trends in NP size support our claim that the proximity of M-ox to the C-terminus can be varied to affect particle metrics.

Ultimately, our primary motive in this work is to establish molecular methods of adjusting the structure and chiroptical signal intensity of helical AuNP superstructures. In theory, single-helical superstructures assembled from large oblong particles should exhibit intense optical chirality measured by their CD signal and anisotropy factor (g). We have previously reported that single helices derived from C_{18}-$(PEP_{Au}^{M\text{-}ox,9})_2$ typically exhibit a g-factor ~0.017.[10a] To obtain higher g-factor values in this system, modified synthetic conditions are required to increase AuNP size.[2g] Helices derived from C_{18}-$(PEP_{Au}^{M\text{-}ox,11})_2$, which consist of significantly larger oblong particles, simply due to a shift in M-ox position, display a more intense CD signal (Figure 4f). The corresponding absolute g-factor is measured to be ~0.37. Further optimization of synthetic conditions might result in even higher g-factor values.

CONCLUSION

By combining theory and experiment, we demonstrate that encoding chemical information in PEP_{Au}-based assembly agents via sequence engineering is a highly effective method of affecting nanoscale structure and optimizing chiroptical properties of AuNP single helices. We envision that other regions within the PEP_{Au} sequence, such as the β-sheet region, could be similarly tuned to affect the nanoscale properties of chiral helical gold nanoparticle superstructures.

DOI: 10.1021/jacs.9b08798
J. Am. Chem. Soc. 2019, 141, 15710−15716

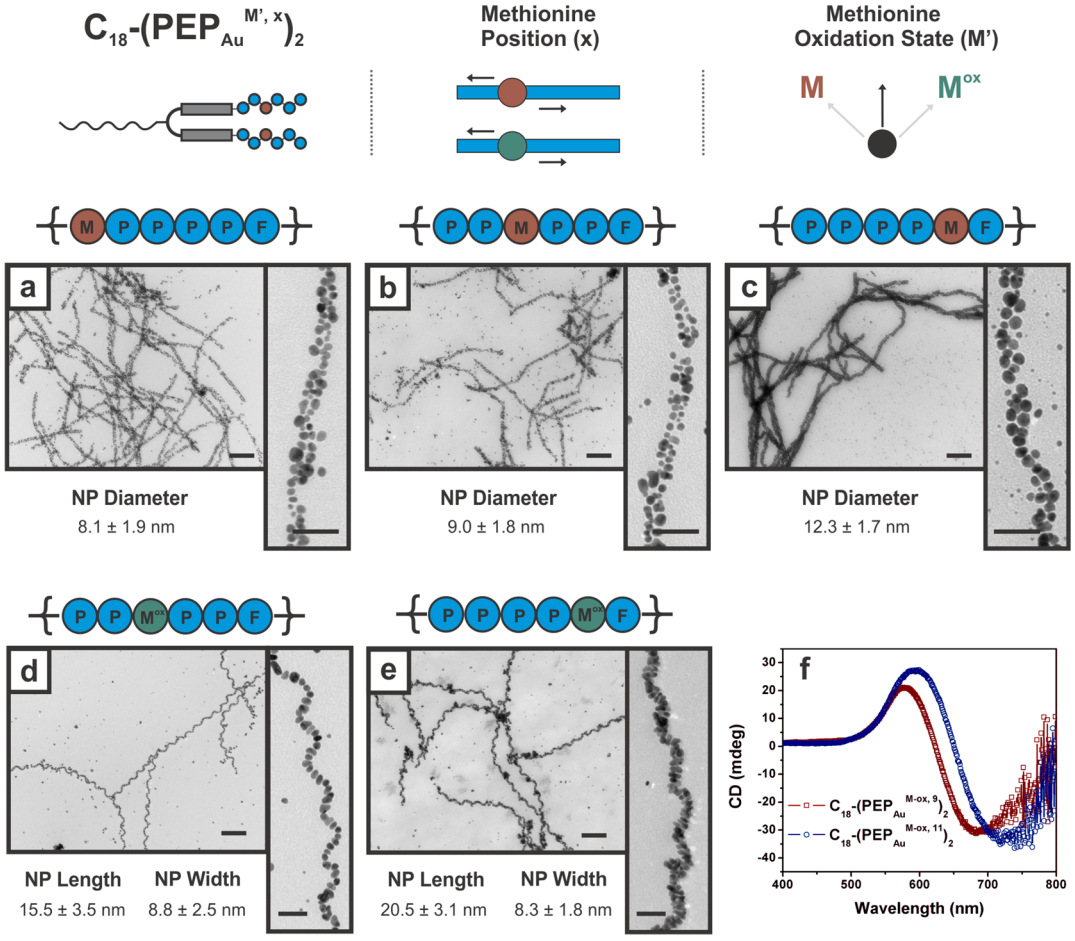

Figure 4. Effect of methionine modification on the size and shape of component AuNPs within helical superstructures. TEM analysis of 1-D superstructures constructed using (a) C_{18}-($PEP_{Au}^{M,7}$)$_2$, (b) C_{18}-($PEP_{Au}^{M,9}$)$_2$, and (c) C_{18}-($PEP_{Au}^{M,11}$)$_2$. Average NP diameters of component NPs in each case are listed below the corresponding TEM image. TEM characterization of single-helical AuNP superstructures constructed using (d) C_{18}-($PEP_{Au}^{M\text{-}ox,9}$)$_2$ and (e) C_{18}-($PEP_{Au}^{M\text{-}ox,11}$)$_2$. (f) The chiroptical signal derived from C_{18}-($PEP_{Au}^{M\text{-}ox,11}$)$_2$-based helices is more intense as compared to the signal derived from C_{18}-($PEP_{Au}^{M\text{-}ox,9}$)$_2$-based helices. Low magnification images scale bar = 200 nm, and high magnification images scale bar = 50 nm.

EXPERIMENTAL METHODS

General Methods and Materials. All chemicals were obtained from commercial sources and used without further purification. All peptides were synthesized using established microwave-assisted solid-phase peptide synthesis protocols on a CEM Mars microwave. Nanopure water (18.1 mΩ) from Barnstead DiamondTM water purification system was used to prepare all aqueous solutions. Peptides were purified by reverse-phase high-performance liquid chromatography on Agilent 1200 liquid chromatographic system equipped with diode array and multiple wavelength detectors using a Zorbax-300SB C_{18} column. Peptide masses were confirmed by liquid chromatography−mass spectrometry (LC−MS) data using Shimadzu LC-MS 2020. UV−vis spectra were collected using an Agilent 8453 UV−vis spectrometer with a quartz cuvette (10 mm path length). All microscopy measurements were made using ImageJ software.

Synthesis. *Peptide Synthesis.* All peptides were synthesized via established microwave-assisted solid-phase peptide synthesis protocols. Briefly, 138.8 mg (0.025 mmol) of Fmoc-Phe-NovasynR TGA resin (Millipore catalogue number: 8560340001) was soaked in DMF for 15 min. To begin the cycle of reactions, Fmoc-deprotection of the resin was performed by adding 2 mL of 20% 4-methylpiperidine in DMF to the resin and heating the mixture to 75 °C in 1 min and holding at that temperature for 2 min. Excess reagent was drained using a filtration manifold and washed with copious amounts of DMF. To couple individual amino acids, 0.1 M solution of HCTU in NMP (5 equiv to resin, 1.25 mL) was added to Fmoc-protected amino acid (4 equiv, 0.125 mmol) followed by DIEA (7 equiv, 0.175 mmol, 30.4 μL). The resulting solution was vortexed and centrifuged to ensure complete dissolution of amino acid. Thereafter, the solution was transferred to resin and heated to 75 °C for 1 min and held at that temperature for 5 min. Excess reagent was then again drained, and the resin was washed with copious amounts of DMF. This cycle of reactions was repeated for every amino acid. Proline and adjacent amino acid were coupled twice to ensure complete reaction of secondary amide group. The N-terminus was capped with 5-azido pentanoic acid using the same synthetic steps described above.

Peptide Conjugate Synthesis. C_{18}-dialkyne was attached to each azido peptide sequence via Cu-catalyzed click chemistry, which is described in our previous publications.[2g,10b]

Nanoparticle Synthesis and Assembly. *Discrete Nanoparticle Synthesis.* Synthetic conditions used to prepare discrete NPs in the presence of peptides were based on a previously established protocol.[9] $PEP_{Au}^{M,x}$ and $PEP_{Au}^{M\text{-}ox,x}$ (x = 7, 9, 11) were dissolved in 250 μL of 0.1 M HEPES. Next, 2 μL of 0.1 M $HAuCl_4$ solution was added to the peptide−HEPES mixture. The reaction mixture was quickly vortexed after observance of a black precipitate (∼4−5 s after adding the gold source), and thereafter the reaction vial was left undisturbed on the bench.

Nanoparticle Superstructure Assembly. 18.725 nmol of C_{18}-($PEP_{Au}^{M,x}$)$_2$ and C_{18}-($PEP_{Au}^{M\text{-}ox,x}$)$_2$ (x = 7, 9, 11) was dissolved in 250 μL of 0.1 M HEPES buffer, sonicated for 5 min, and allowed to sit for 25 min. Thereafter, 2 μL of 1:1 mixture of aqueous 0.1 M $HAuCl_4$ in 1 M TEAA buffer was added to the peptide−HEPES mixture. About

DOI: 10.1021/jacs.9b08798
J. Am. Chem. Soc. 2019, 141, 15710−15716

2−3 s after addition of gold precursor solution, a black precipitate emerged, and then the solution was immediately vortexed. The reaction vial was thereafter left undisturbed on the bench.

Characterization and Sample Preparation. *Circular Dichroism Spectroscopy.* CD measurements were performed on an Olis DSM 17 CD spectrometer with a quartz cuvette (0.1 cm path length) at 25 °C with 8 nm/min scan rate. The concentration of the peptide in 10 mM HEPES buffer solution was 75 μM.

Atomic Force Microscopy. AFM measurements were performed in tapping mode using an Asylum MFP-3D atomic force microscope and ultrasharp AFM tips (NanoandMore SHR-150). 0.1% APTES (3-aminopropyl-triethoxy-silane) solution was drop casted onto a freshly cut mica surface, followed by rinsing with Nanopure water. 50 μL of peptide−HEPES solution in 0.1 M HEPES (75 μM) was then drop cast and rinsed with water after 1 min and allowed to dry in the desiccator overnight.

Transmission Electron Microscopy. TEM was conducted on a FEI Morgagni 268 operated at 80 kV using an AMT side mount CCD camera system. Six microliters of peptide conjugate solution was drop casted onto a 3 mm-diameter copper grid with Formvar coating. After 5 min, excess solution was wicked away, and the grid was air-dried for 2 min. Thereafter, 6 μL of Nanopure water was drop cast onto the grid and allowed to sit for 30 s. Excess solution was wicked away, and the grid was allowed to air-dry for 5 min.

Molecular Simulations. *Replica-Exchange with Solute Tempering Molecular Dynamics Simulations.* REST-MD simulations[15] were used to predict the Boltzmann-weighted ensemble of configurations for each of the six peptide sequences, in both the surface-adsorbed and the unadsorbed states. Each unadsorbed simulation comprised one of the six peptides and liquid water. Each surface-adsorbed simulation comprised these and also a Au surface, modeled as a Au(111) slab five atomic layers thick. The Au(111) substrate has been previously demonstrated to be an effective approximation for more complex Au surfaces.[18,19] The peptide, Au surface, and water were modeled using the CHARMM-22*,[20] GolP-CHARMM,[16] and modified TIP3P[21] potentials, respectively. Periodic boundary conditions were used in 3D. Frames were saved from each trajectory every 1 ps. These trajectories were analyzed using clustering with respect to the relative positions of the peptide backbone atoms. In addition, for the surface-adsorbed simulations, we applied a residue−surface contact analysis, which yielded the percentage of frames that each residue was in contact with the surface. Full details of the simulations and analyses are provided in the Supporting Information.

First-Principles Calculations. Plane-wave density functional theory calculations were carried out for dimethyl sulfoxide adsorbed onto the Au(111) surface in vacuo, using Quantum Espresso (v5.2.0).[22] Three-dimensional periodic boundary conditions were employed using a $3 \times 3\sqrt{3}$ supercell and a Au slab four atomic layers thick. Calculations were performed using vdW-DF[13] with the revPBE exchange-correlation functional.[23] The binding energy of dimethyl sulfoxide was determined via two stages: a geometry optimization followed by a single point energy calculation of the resultant geometry. The binding energy was calculated using the supermolecule approach. Full details are provided in the Supporting Information.

■ ASSOCIATED CONTENT

Supporting Information

The Supporting Information is available free of charge on the ACS Publications website at DOI: 10.1021/jacs.9b08798.

LC−MS, TEM, CD, AFM, and additional computational data (PDF)

■ AUTHOR INFORMATION

Corresponding Authors

*tiffany.walsh@deakin.edu.au
*nrosi@pitt.edu

ORCID

Soumitra Mokashi-Punekar: 0000-0002-4322-4421
Tiffany R. Walsh: 0000-0002-0233-9484
Nathaniel L. Rosi: 0000-0001-8025-8906

Notes

The authors declare no competing financial interest.

■ ACKNOWLEDGMENTS

We are grateful for financial support from the National Science Foundation (DMR-1904960, N.L.R.). S.M.-P. acknowledges an Andrew Mellon Predoctoral Fellowship awarded by the University of Pittsburgh. T.R.W. gratefully acknowledges computing resources provided by the National Computing Infrastructure, Canberra, and the Pawsey Supercomputing Centre, Perth, Australia.

■ REFERENCES

(1) (a) Mirkin, C. A.; Letsinger, R. L.; Mucic, R. C.; Storhoff, J. J. A DNA-Based Method for Rationally Assembling Nanoparticles into Macroscopic Materials. *Nature* **1996**, *382*, 607−609. (b) Nikoobakht, B.; Wang, Z. L.; El-Sayed, M. A. Self-Assembly of Gold Nanorods. *J. Phys. Chem. B* **2000**, *104*, 8635−8640.

(2) (a) Chen, C.-L.; Zhang, P.; Rosi, N. L. A New Peptide-Based Method for the Design and Synthesis of Nanoparticle Superstructures: Construction of Highly Ordered Gold Nanoparticle Double Helices. *J. Am. Chem. Soc.* **2008**, *130*, 13555−13557. (b) Sharma, J.; Chhabra, R.; Cheng, A.; Brownell, J.; Liu, Y.; Yan, H. Control of Self-Assembly of DNA Tubules Through Integration of Gold Nanoparticles. *Science* **2009**, *323*, 112−116. (c) Guerrero-Martínez, A.; Auguié, B.; Alonso-Gómez, J. L.; Džolić, Z.; Gómez-Graña, S.; Žinić, M.; Cid, M. M.; Liz-Marzán, L. M. Intense Optical Activity from Three-Dimensional Chiral Ordering of Plasmonic Nanoantennas. *Angew. Chem., Int. Ed.* **2011**, *50*, 5499−5503. (d) Kuzyk, A.; Schreiber, R.; Fan, Z.; Pardatscher, G.; Roller, E.-M.; Hogele, A.; Simmel, F. C.; Govorov, A. O.; Liedl, T. DNA-Based Self-Assembly of Chiral Plasmonic Nanostructures with Tailored Optical Response. *Nature* **2012**, *483*, 311−314. (e) Song, C.; Blaber, M. G.; Zhao, G.; Zhang, P.; Fry, H. C.; Schatz, G. C.; Rosi, N. L. Tailorable Plasmonic Circular Dichroism Properties of Helical Nanoparticle Superstructures. *Nano Lett.* **2013**, *13*, 3256−3261. (f) Urban, M. J.; Dutta, P. K.; Wang, P.; Duan, X.; Shen, X.; Ding, B.; Ke, Y.; Liu, N. Plasmonic Toroidal Metamolecules Assembled by DNA Origami. *J. Am. Chem. Soc.* **2016**, *138*, 5495−5498. (g) Merg, A. D.; Boatz, J. C.; Mandal, A.; Zhao, G.; Mokashi-Punekar, S.; Liu, C.; Wang, X.; Zhang, P.; van der Wel, P. C. A.; Rosi, N. L. Peptide-Directed Assembly of Single-Helical Gold Nanoparticle Superstructures Exhibiting Intense Chiroptical Activity. *J. Am. Chem. Soc.* **2016**, *138*, 13655−13663. (h) Ma, W.; Xu, L.; de Moura, A. F.; Wu, X.; Kuang, H.; Xu, C.; Kotov, N. A. Chiral Inorganic Nanostructures. *Chem. Rev.* **2017**, *117*, 8041−8093. (i) Lan, X.; Lu, X.; Shen, C.; Ke, Y.; Ni, W.; Wang, Q. Au Nanorod Helical Superstructures with Designed Chirality. *J. Am. Chem. Soc.* **2015**, *137*, 457−462.

(3) (a) Wu, X.; Xu, L.; Liu, L.; Ma, W.; Yin, H.; Kuang, H.; Wang, L.; Xu, C.; Kotov, N. A. Unexpected Chirality of Nanoparticle Dimers and Ultrasensitive Chiroplasmonic Bioanalysis. *J. Am. Chem. Soc.* **2013**, *135*, 18629−18636. (b) Ma, W.; Kuang, H.; Xu, L.; Ding, L.; Xu, C.; Wang, L.; Kotov, N. A. Attomolar DNA Detection with Chiral Nanorod Assemblies. *Nat. Commun.* **2013**, *4*, 2689. (c) Kumar, J.; Erana, H.; López-Martínez, E.; Claes, N.; Martín, V. F.; Solís, D. M.; Bals, S.; Cortajarena, A. L.; Castilla, J.; Liz-Marzán, L. M. Detection of Amyloid Fibrils in Parkinson's Disease Using Plasmonic Chirality. *Proc. Natl. Acad. Sci. U. S. A.* **2018**, *115*, 3225−3230.

(4) Shukla, N.; Bartel, M. A.; Gellman, A. J. Enantioselective Separation on Chiral Au Nanoparticles. *J. Am. Chem. Soc.* **2010**, *132*, 8575−8580.

(5) (a) Pendry, J. B. A Chiral Route to Negative Refraction. *Science* **2004**, *306*, 1353−1355. (b) Pendry, J. B. Negative Refraction Makes a

DOI: 10.1021/jacs.9b08798
J. Am. Chem. Soc. 2019, 141, 15710−15716

Perfect Lens. *Phys. Rev. Lett.* **2000**, *85*, 3966−3969. (c) Smith, D. R.; Pendry, J. B.; Wiltshire, M. C. K. Metamaterials and Negative Refractive Index. *Science* **2004**, *305*, 788−792. (d) Gansel, J. K.; Thiel, M.; Rill, M. S.; Decker, M.; Bade, K.; Saile, V.; von Freymann, G.; Linden, S.; Wegener, M. Gold Helix Photonic Metamaterial as Broadband Circular Polarizer. *Science* **2009**, *325*, 1513−1515.

(6) (a) Fan, Z.; Govorov, A. O. Plasmonic Circular Dichroism of Chiral Metal Nanoparticle Assemblies. *Nano Lett.* **2010**, *10*, 2580−2587. (b) Fan, Z.; Govorov, A. O. Helical Metal Nanoparticle Assemblies with Defects: Plasmonic Chirality and Circular Dichroism. *J. Phys. Chem. C* **2011**, *115*, 13254−13261. (c) Govorov, A. O.; Gun'ko, Y. K.; Slocik, J. M.; Gerard, V. A.; Fan, Z.; Naik, R. R. Chiral Nanoparticle Assemblies: Circular Dichroism, Plasmonic Interactions, and Exciton Effects. *J. Mater. Chem.* **2011**, *21*, 16806−16818. (d) Ben-Moshe, A.; Maoz, B. M.; Govorov, A. O.; Markovich, G. Chirality and Chiroptical Effects in Inorganic Nanocrystal Systems with Plasmon and Exciton Resonances. *Chem. Soc. Rev.* **2013**, *42*, 7028−7041.

(7) (a) Chen, C.-L.; Rosi, N. L. Preparation of Unique 1-D Nanoparticle Superstructures and Tailoring their Structural Features. *J. Am. Chem. Soc.* **2010**, *132*, 6902−6903. (b) Hwang, L.; Zhao, G.; Zhang, P.; Rosi, N. L. Size-Controlled Peptide-Directed Synthesis of Hollow Spherical Gold Nanoparticle Superstructures. *Small* **2011**, *7*, 1939−1942. (c) Zhang, C.; Zhou, Y.; Merg, A.; Song, C.; Schatz, G. C.; Rosi, N. L. Hollow Spherical Gold Nanoparticle Superstructures with Tunable Diameters and Visible to Near-Infrared Extinction. *Nanoscale* **2014**, *6*, 12328−12332. (d) Zhang, C.; Song, C.; Fry, H. C.; Rosi, N. L. Peptide Conjugates for Directing the Morphology and Assembly of 1D Nanoparticle Superstructures. *Chem. - Eur. J.* **2014**, *20*, 941−945. (e) Song, C.; Wang, Y.; Rosi, N. L. Peptide-Directed Synthesis and Assembly of Hollow Spherical CoPt Nanoparticle Superstructures. *Angew. Chem., Int. Ed.* **2013**, *52*, 3993−3995.

(8) Song, C. Z. G.; Zhang, P.; Rosi, N. L. Expeditious Synthesis and Assembly of Sub-100 nm Hollow Spherical Gold Nanoparticle Superstructures. *J. Am. Chem. Soc.* **2010**, *132*, 14033−14035.

(9) Slocik, J. M.; Stone, M. O.; Naik, R. R. Synthesis of Gold Nanoparticles Using Multifunctional Peptides. *Small* **2005**, *1*, 1048−1052.

(10) (a) Mokashi-Punekar, S.; Merg, A. D.; Rosi, N. L. Systematic Adjustment of Pitch and Particle Dimensions within a Family of Chiral Plasmonic Gold Nanoparticle Single Helices. *J. Am. Chem. Soc.* **2017**, *139*, 15043−15048. (b) Merg, A. D.; Slocik, J.; Blaber, M. G.; Schatz, G. C.; Naik, R.; Rosi, N. L. Adjusting the Metrics of 1-D Helical Gold Nanoparticle Superstructures Using Multivalent Peptide Conjugates. *Langmuir* **2015**, *31*, 9492−9501.

(11) (a) Bedford, N. M.; Hughes, Z. E.; Tang, Z.; Li, Y.; Briggs, B. D.; Ren, Y.; Swihart, M. T.; Petkov, V. G.; Naik, R. R.; Knecht, M. R.; Walsh, T. R. Sequence-Dependent Structure/Function Relationships of Catalytic Peptide-Enabled Gold Nanoparticles Generated under Ambient Synthetic Conditions. *J. Am. Chem. Soc.* **2016**, *138*, 540−548. (b) Tang, Z.; Palafox-Hernandez, J. P.; Law, W.-C.; Hughes, Z. E.; Swihart, M. T.; Prasad, P. N.; Knecht, M. R.; Walsh, T. R. Biomolecular Recognition Principles for Bionanocombinatorics: An Integrated Approach to Elucidate Enthalpic and Entropic Factors. *ACS Nano* **2013**, *7*, 9632−9646.

(12) Habib, A.; Tabata, M.; Wu, Y. G. Formation of Gold Nanoparticles by Good's Buffers. *Bull. Chem. Soc. Jpn.* **2005**, *78*, 262−269.

(13) (a) Dion, M.; Rydberg, H.; Schroder, E.; Langreth, D. C.; Lundqvist, B. I. Van der Waals Density Functional for General Geometries. *Phys. Rev. Lett.* **2004**, *92*, 246401. (b) Thonhauser, T.; Cooper, V. R.; Li, S.; Puzder, A.; Hyldgaard, P.; Langreth, D. C. Van der Waals Density Functional: Self-Consistent Potential and the Nature of the van der Waals Bond. *Phys. Rev. B: Condens. Matter Mater. Phys.* **2007**, *76*, 125112. (c) Roman-Perez, G.; Soler, J. M. Efficient Implementation of a van der Waals Density Functional: Application to Double-Wall Carbon Nanotubes. *Phys. Rev. Lett.* **2009**, *103*, 096102.

(14) Wright, L. B.; Roger, P. M.; Walsh, T. R.; Corni, S. First-Principles-Based Force Field for the Interaction of Proteins with Au(100)(5 × 1): An Extension of GolP-CHARMM. *J. Phys. Chem. C* **2013**, *117*, 24292−24306.

(15) (a) Terakawa, T.; Kameda, T.; Takada, S. On Easy Implementation of a Variant of the Replica Exchange with Solute Tempering in GROMACS. *J. Comput. Chem.* **2011**, *32*, 1228−1234. (b) Wright, L. B.; Walsh, T. R. Efficient Conformational Sampling of Peptides Adsorbed onto Inorganic Surfaces: Insights from a Quartz Binding Peptide. *Phys. Chem. Chem. Phys.* **2013**, *15*, 4715−4726.

(16) Wright, L. B.; Rodger, P. M.; Corni, S.; Walsh, T. R. GolP-CHARMM: First-Principles Based Force Fields for the Interaction of Proteins with Au(111) and Au(100). *J. Chem. Theory Comput.* **2013**, *9*, 1616−1630.

(17) Wright, L. B.; Palafox-Hernandez, J. P.; Rodger, P. M.; Corni, S.; Walsh, T. R. Facet Selectivity in Gold Binding Peptides: Exploiting Interfacial Water Structure. *Chem. Sci.* **2015**, *6*, 5204−5214.

(18) Hughes, Z. E.; Nguyen, M. A.; Li, Y.; Swihart, M. T.; Walsh, T. R.; Knecht, M. R. Elucidating the Influence of Materials-Binding Peptide Sequence on Au Surface Interactions and Colloidal Stability of Au Nanoparticles. *Nanoscale* **2017**, *9*, 421−432.

(19) Hughes, Z. E.; Kochandra, R.; Walsh, T. R. Facet-Specific Adsorption of Tripeptides at Aqueous Au Interfaces: Open Questions in Reconciling Experiment and Simulation. *Langmuir* **2017**, *33*, 3742−3754.

(20) (a) MacKerell, A. D.; Bashford, D.; Bellott, M.; Dunbrack, R. L.; Evanseck, J. D.; Field, M. J.; Fischer, S.; Gao, J.; Guo, H.; Ha, S.; Joseph-McCarthy, D.; Kuchnir, L.; Kuczera, K.; Lau, F. T. K.; Mattos, C.; Michnick, S.; Ngo, T.; Nguyen, D. T.; Prodhom, B.; Reiher, W. E.; Roux, B.; Schlenkrich, M.; Smith, J. C.; Stote, R.; Straub, J.; Watanabe, M.; Wiórkiewicz-Kuczera, J.; Yin, D.; Karplus, M. All-Atom Empirical Potential for Molecular Modeling and Dynamics Studies of Proteins. *J. Phys. Chem. B* **1998**, *102*, 3586−3616. (b) Piana, S.; Lindorff-Larsen, K.; Shaw, D. E. How Robust Are Protein Folding Simulations with Respect to Force Field Parameterization? *Biophys. J.* **2011**, *100*, L47−L49.

(21) (a) Jorgensen, W. L.; Chandrasekhar, J.; Madura, J. D.; Impey, R. W.; Klein, M. L. Comparison of Simple Potential Functions for Simulating Liquid Water. *J. Chem. Phys.* **1983**, *79*, 926−935. (b) Neria, E.; Fischer, S.; Karplus, M. Simulation of Activation Free Energies in Molecular Systems. *J. Chem. Phys.* **1996**, *105*, 1902−1921.

(22) Giannozzi, P.; Baroni, S.; Bonini, N.; Calandra, M.; Car, R.; Cavazzoni, C.; Ceresoli, D.; Chiarotti, G. L.; Cococcioni, M.; Dabo, I.; Corso, A. D.; de Gironcoli, S.; Fabris, S.; Fratesi, G.; Gebauer, R.; Gerstmann, U.; Gougoussis, C.; Kokalj, A.; Lazzeri, M.; Martin-Samos, L.; Marzari, N.; Mauri, F.; Mazzarello, R.; Paolini, S.; Pasquarello, A.; Paulatto, L.; Sbraccia, C.; Scandolo, S.; Sclauzero, G.; Seitsonen, A. P.; Smogunov, A.; Umari, P.; Wentzcovitch, R. M. QUANTUM ESPRESSO: A Modular and Open-Source Software Project for Quantum Simulations of Materials. *J. Phys.: Condens. Matter* **2009**, *21*, 395502.

(23) Hammer, B.; Hansen, L. B.; Norskov, J. K. Improved Adsorption Energetics Within Density-Functional Theory Using Revised Perdew-Burke-Ernzerhof Functionals. *Phys. Rev. B: Condens. Matter Mater. Phys.* **1999**, *59*, 7413−7421.

DOI: 10.1021/jacs.9b08798
J. Am. Chem. Soc. 2019, 141, 15710−15716